Chapter 2

Size Effect in Concrete Structures

ROLF ELIGEHAUSEN & JOŠKO OŽBOLT
Institut für Werkstoffe im Bauwesen, Universität Stuttgart,
Pfaffenwaldring 4, 7000 Stuttgart 80, Germany

ABSTRACT

The size effect for notched-tension specimens, three-point bend specimens, pull-out headed anchor specimens and beams loaded in torsion are calculated using a 2D and 3D finite element program. The program is based on the nonlocal microplane model. The calculated failure loads are compared with previously obtained experimental results. Test results and calculated data are compared with the recently proposed size effect law. Results of tests and analysis exhibit significant size effect that should be taken into account in design practice. It is demonstrated that the nonlocal microplane model used in a 2D and 3D finite element code can correctly predict failure loads for similar specimens of different sizes.

1. INTRODUCTION

The size effect in concrete structures is a well known phenomenon. For example, the bending strength decreases with increasing specimen height. Another example is the shear strength of concrete beams without shear reinforcement. Kani [1] was one of the first to demonstrate that the shear strength of identical concrete beams decreases with increasing beam depth and that the shear design provisions used at that time were unsafe for larger beams. This size effect can well be explained by fracture mechanics, because the

fracture in a concrete structure is driven by the stored elastic energy that is released globally from the entire structure. However, before failure, microcracking in the concrete causes deviations of the size effect from the geometrical size effect known from linear elastic fracture mechanics (LEFM), because for normal geometrical sizes the fracture process zone is relatively large with regard to the geometry of the structure and therefore the size effect can only be correctly calculated using nonlinear fracture mechanics (NLFM).

In numerical analysis it is very difficult to model damage and fracture processes in materials such as concrete correctly. At present, three different material models for strain-softening damage exists:

(1) Continuum models used together with fracture mechanics.
(2) Random particle model, in which the microstructure is imagined to consist of randomly arranged rigid aggregate pieces with elastic-softening interactions between them.
(3) Micro-finite element models, in which the matrix as well as the aggregate pieces in concrete are subdivided into many finite elements, whose inelastic behaviour and cracking as well as interface bond failures are taken into account.

The last two material models automatically take into account the structural size effect but they are still extremely demanding of computer time and cannot be used in structural analysis. Therefore, the continuum material models must be formulated in such a way that they are capable of describing fracture of the structure in a correct way.

In the present study a number of finite element analyses are performed to investigate the structural size effect. A continuum material model, called the *nonlocal microplane model,* based on the smeared crack approach is used. Numerical studies of the structural size effect are presented and discussed for plain concrete specimens loaded in centric tension, three-point bending, axisymmetric pull-out of headed anchors and beam torsion. The calculated results are compared with available test data as well as with the size effect law recently proposed by Bažant [2].

2. SUMMARY OF NONLOCAL MICROPLANE MODEL FOR CONCRETE

The microplane models were initiated by Taylor [3], who suggested the principle for the modelling of plasticity of polycrystalline metals.

In that approach, developed in detail by Batdorf & Budianski [4] and others, the plastic slips were calculated independently on various crystallographic planes based on the resolved shear stress component, and were then superimposed to obtain the plastic microstrain. Later this approach was extended, under the name multilaminate model, to the modelling of non-softening plastic response of soils or rocks [5]. Recently [6]–[9], this approach was extended to include strain softening of concrete, and was renamed more generally as the *microplane model,* in recognition of the fact that the approach is not limited to plastic slip but can equally well describe cracking and strain-softening damage. To prevent instability due to strain softening, the microplanes must be constrained kinematically rather than statically, in which case the use of the principle of virtual work must replace the direct superposition of the plastic strains as used in the slip theory.

In the present study the microplane model originally developed by Bažant & Prat [9], is slightly modified and implemented into a 2D and 3D finite element code. The basic hypotheses used in the model are as follows:

Hypothesis I—The strains on any microplane represent the resolved components of the macrostrain tensor ε_{ij} (kinematic constrains).

Hypothesis II—Each microplane resists not only normal strain ε_N, but also shear strain ε_T. Shear strain is split into two mutually perpendicular in-plane components and as a consequence the shear stress vector is not parallel with the shear strain vector. This is the main modification in contrast to the originally proposed microplane model [9], where stress and strain vectors are parallel.

Hypothesis III—The normal microplane strain is split into volumetric and deviatoric components, i.e. $\varepsilon_N = \varepsilon_V + \varepsilon_D$.

Hypothesis IV—The stress–strain relation for each microplane is path independent as long as there is no unloading on this microplane for that component. During each unloading and reloading, which is defined separately in each microplane, the curves of the stress and strain differences from the state at the start of the unloading are also path independent. Thus, all the macroscopic path dependence is produced by various combinations of loading and unloading on all the microplanes.

Hypothesis V—The volumetric, deviatoric and shear responses on each microplane are mutually independent.

These five hypotheses were shown to allow an excellent representation of nonlinear test data for concrete in 1D, 2D and 3D stress–strain states [9].

A basic requirement for a continuum model for a brittle heterogeneous material such as concrete is that it must correctly display the consequences of heterogeneity of the microstructure. A continuum constitutive model lumps the average response of a certain characteristic volume of the material (Fig. 1). In essence, one may distinguish two types of interactions among the particles or damage sites in the microstructure, which must be somehow manifested in the continuum model: (1) Interaction at a distance *among various sites* (e.g. between A and B, Fig. 1); and (2) interaction *among various orientations* (see angle α in Fig. 1).

The interactions at a distance control the localization of damage. They are ignored in the classical, local continuum models but are reflected in nonlocal models [10]. The nonlocal aspect is a requisite for a realistic description of the size effect, as well as for the modelling of fracture propagation in the form of a crack band.

According to the nonlocal concept, the stress at a point depends not only on the strain at the same point but also on the strain field in a certain neighbourhood of the point [11]–[14]. For strain-softening behaviour, this concept was introduced by Bažant *et al.* [15]. In the current study, an effective form of the nonlocal concept, in which all variables that are associated with strain softening are nonlocal and all other variables are local, is used. The originally proposed nonlocal concept [10], is here modified by introducing additional weighting functions that control averaging into the directions of the main principle stresses. An important advantage of this formulation, called

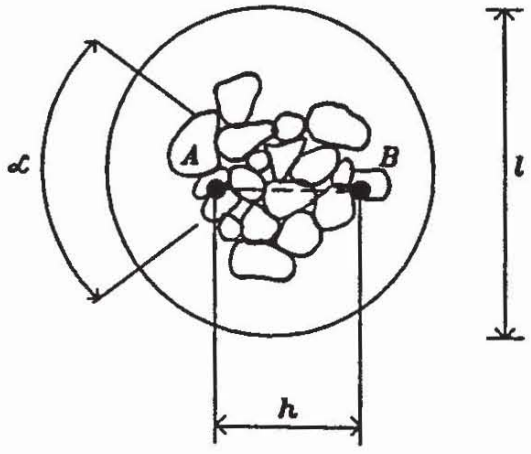

Fig. 1 Interaction among the various orientations and interaction at a distance.

nonlocal damage or nonlocal continuum with local strain, is that the differential equations of equilibrium as well as the boundary conditions are of the same form as in the local continuum theory, and that there exist no zero-energy periodic modes of instability.

The key parameter in the nonlocal concept used is the characteristic length l_c over which the strains are averaged, because it has a significant influence on the results of the analysis. Bažant & Pijaudier-Cabot [16] assumed that this length is a material parameter which can be correlated with G_F and approximately taken as $3d_a$ (d_a = maximum aggregate size) in the case of uniaxial macroscopic stress–strain state. However, presently in general 3D stress–strain situations, the concrete fracture property cannot be measured and correlated with the characteristic length. As a consequence, l_c is difficult to interpret as a material parameter depending on the concrete mix only, but may be influenced by other parameters as well. Further studies are needed to clarify whether this length depends only on the concrete composition or also on other parameters such as strain conditions in the failure zone. Therefore in the current study, in general, the characteristic length was determined such that together with the assumed tension strain-softening relationship, the failure load of a certain type of specimen with given size was correctly matched. Then, in the analysis of the specimens of different sizes, this characteristic length was taken as constant. Only in the analysis of the pull-out specimen was the characteristic length taken arbitrarily as $l_c = 12$ mm.

In a preceding paper [17], the nonlocal microplane model as well as an effective numerical iterative algorithm for the loading steps, that is used in the finite element code, is described in detail.

3. NUMERICAL STUDIES

To demonstrate that the nonlocal microplane model, implemented in the 2D and 3D finite element code, can correctly predict the failure load of plain concrete specimens of different sizes, numerical studies of four cases are presented (Fig. 2):

(1) notched tension specimen;
(2) three-point bend specimen;
(3) pull-out specimen with headed anchors;
(4) torsion of short beams.

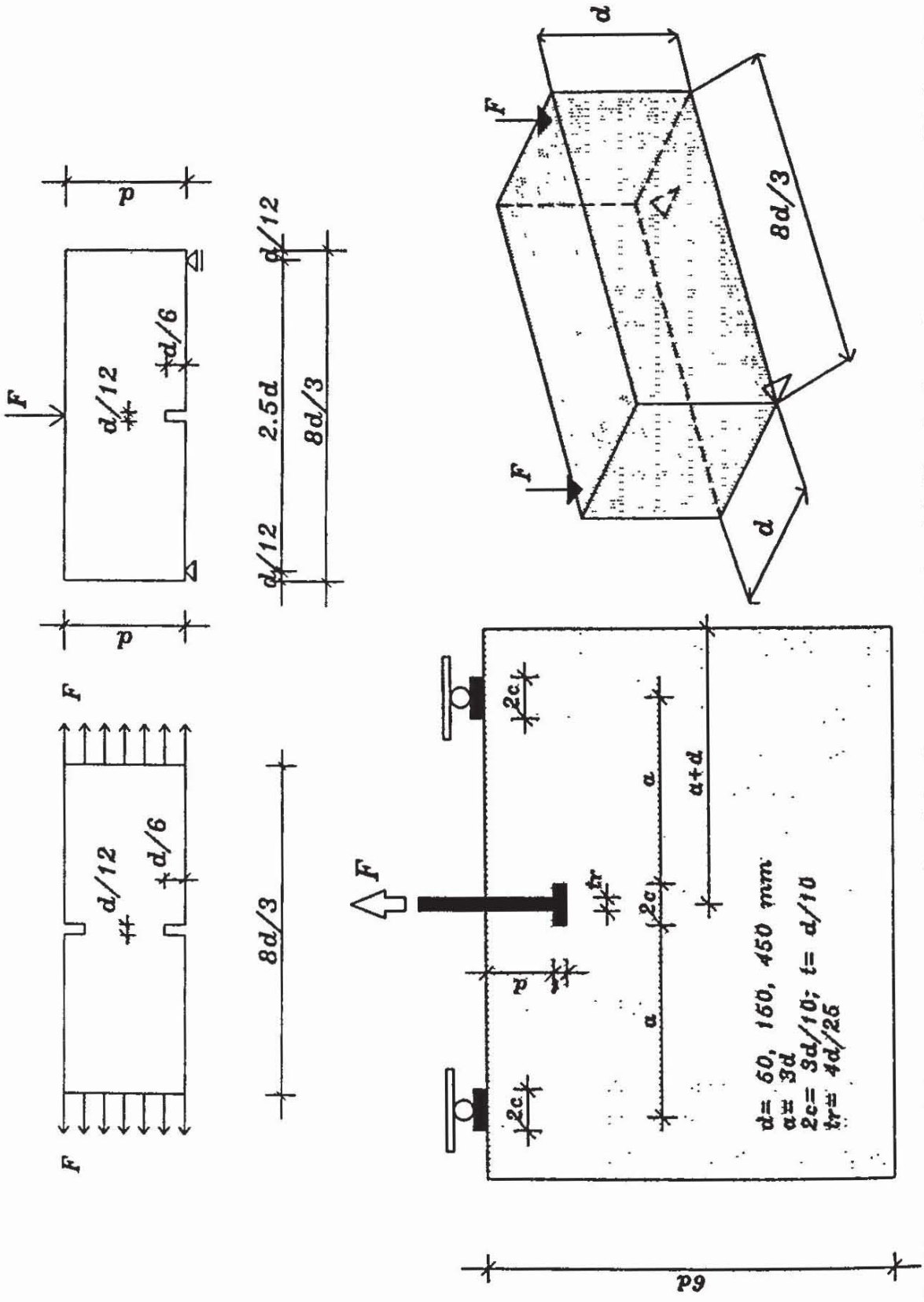

Fig. 2 Geometry of the specimens analysed in the present study. (a) Notched tension specimen; (b) 3-point bend specimen; (c) headed stud anchor; (d) torsion specimen.

In all examples, specimens of three different sizes, in the size ratio 1:2:4, with geometrically similar shapes are used. Exception is made in example (3) where a size ratio of 1:3:9 is studied. Cases (1) and (2) are analysed using four-node plane stress isoparametric finite elements with two by two integration rule. The analysis of the pull-out specimen is made using four-node axisymmetric finite elements with two by two integration rule. Finally, in the torsion problem, eight-node finite elements are employed with two by two by two (smallest specimen) and three by three by three integration rule, respectively. All specimens in the analysis are loaded by prescribing displacement increments in each loading step.

Microplane model parameters in cases (1), (2) and (4) are determined so that they represent the concrete properties used in the experiments. In all the examples the shape of the tension stress–strain curve is determined so that the fracture energy G_F for the unit area of a specimen of length 360 mm is approximately 0·1 N/mm.

Example (2) has been analysed by Bažant & Ožbolt [17], but was re-analysed using slightly different material parameters. Example (3) has been analysed by Eligenausen & Ožbolt [18], and results are shown from this work.

Example (1)—The notched tension specimen shown in Fig. 2(a) is considered. This type of specimen was tested by Bažant & Pfeiffer [19] using concrete with maximum aggregate size $d_a = 12{\cdot}7$ mm. The depth of the smallest specimen was $d = 38{\cdot}1$ mm, the depth of the notch was always 1/6 of the depth of the specimen and the thickness of the specimen was constant for all sizes, $b = 19$ mm. In the analysis only one half of the specimen is modelled. The finite element meshes are shown in Fig. 3 in the deformed state. The characteristic length is taken as $l_c = 3d_a = 38{\cdot}1$ mm. The microplane model parameters are taken so that the calculated tension strength is $f_t = 2{\cdot}70$ MPa. In the experiment the estimated average tension strength, calculated on the basis of the measured uniaxial compressive strength, was $f_t = 2{\cdot}69$ MPa. The characteristic length is chosen such that together with the microplane material parameters, the average failure load of the specimen with $d = 76{\cdot}2$ mm is matched.

In Fig. 4 the nominal stresses at failure related to the total area $\sigma_N = F_U/bd$ (F_U = peak load), obtained in the numerical analysis and in the experiments (average values) are compared with the size effect

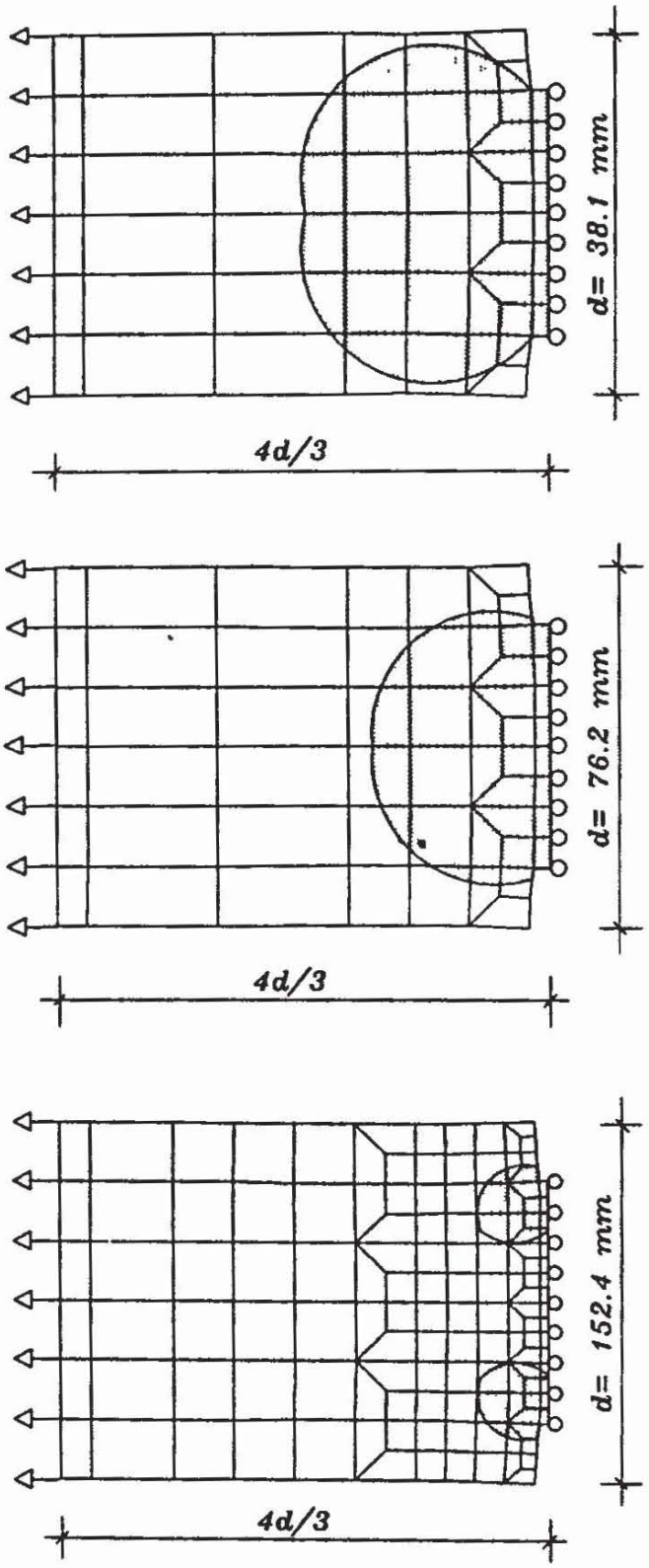

Fig. 3 Deformed finite element meshes and fracture process zone (shaded areas) at peak load for the notched tension specimen.

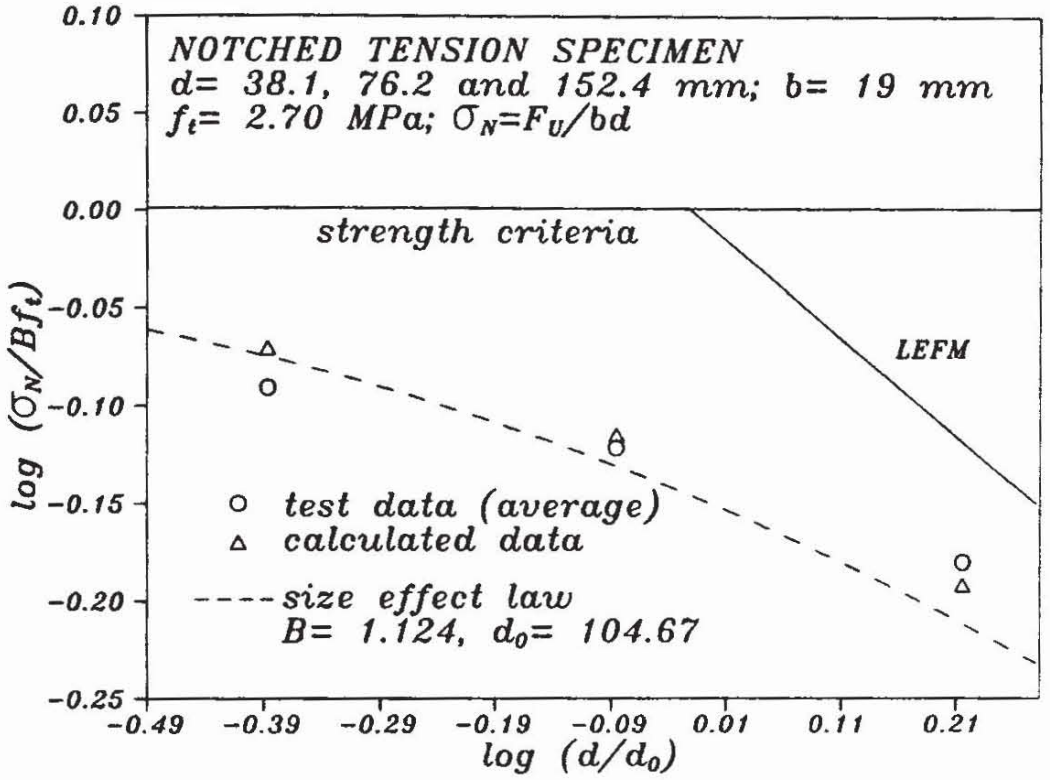

Fig. 4 Comparison between calculated and measured failure loads with size effect law for the notched tension specimen.

law is proposed by Bažant [2]:

$$\sigma_N = Bf_t(1+\beta)^{-1/2} \qquad \beta = d/d_0 \tag{1}$$

The optimum values for the parameters B and d_0 are obtained by linear regression of the numerical results (Fig. 5). In Fig. 6 the nominal stresses at failure (numerical and experimental results) are plotted as a function of the specimen depth in normal scale.

It can be seen from Figs 4–6 that the numerical and experimental results indicate a size effect: the nominal stresses at peak load decrease with increasing specimen depth, that means the absolute failure loads increase approximately by a factor of 1·5 when doubling the depth, much less than the increase in failure area.

In Fig. 3 the shaded areas indicate zones where the tensile stress at peak load exceeds approximately 75% of the uniaxial tensile strength. According to the assumed stress–strain relationship, the concrete starts to exhibit nonlinear behaviour for stresses $\sigma > 0{\cdot}75f_t$. Therefore the shaded area can be assumed as the size of the fracture process zone at peak load. Note that the scale for the specimens of different sizes is inversely proportional to the specimen depth. It is evident from

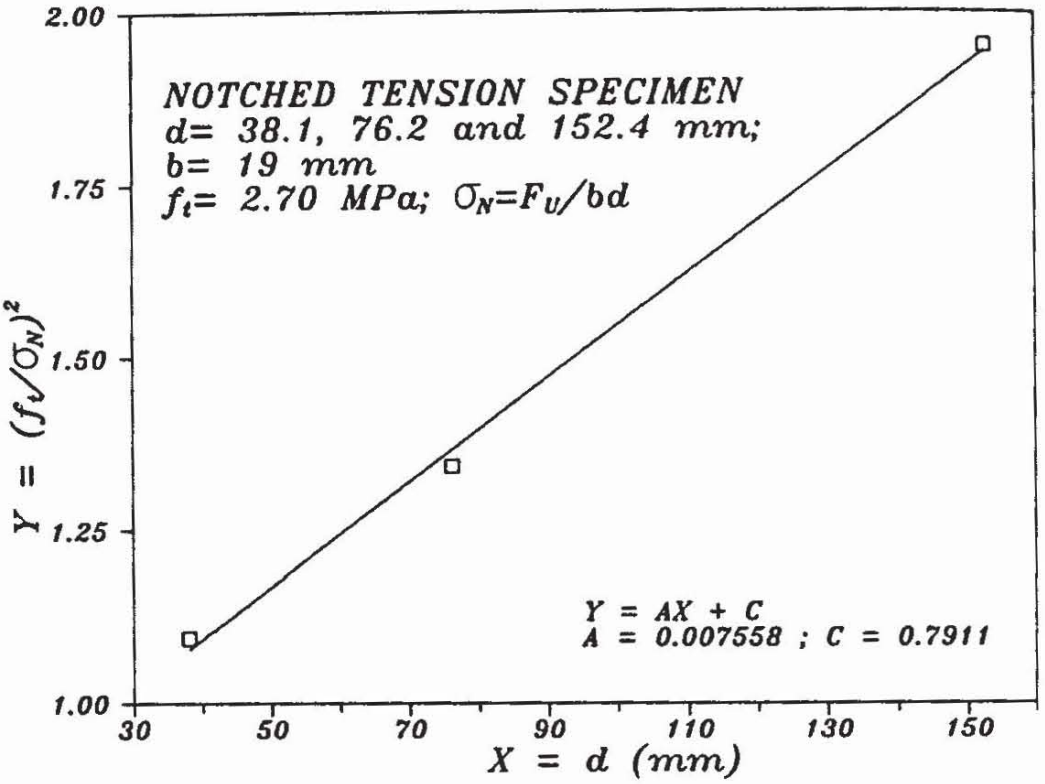

Fig. 5 Linear regression analysis of the calculated peak loads for the notched tension specimen.

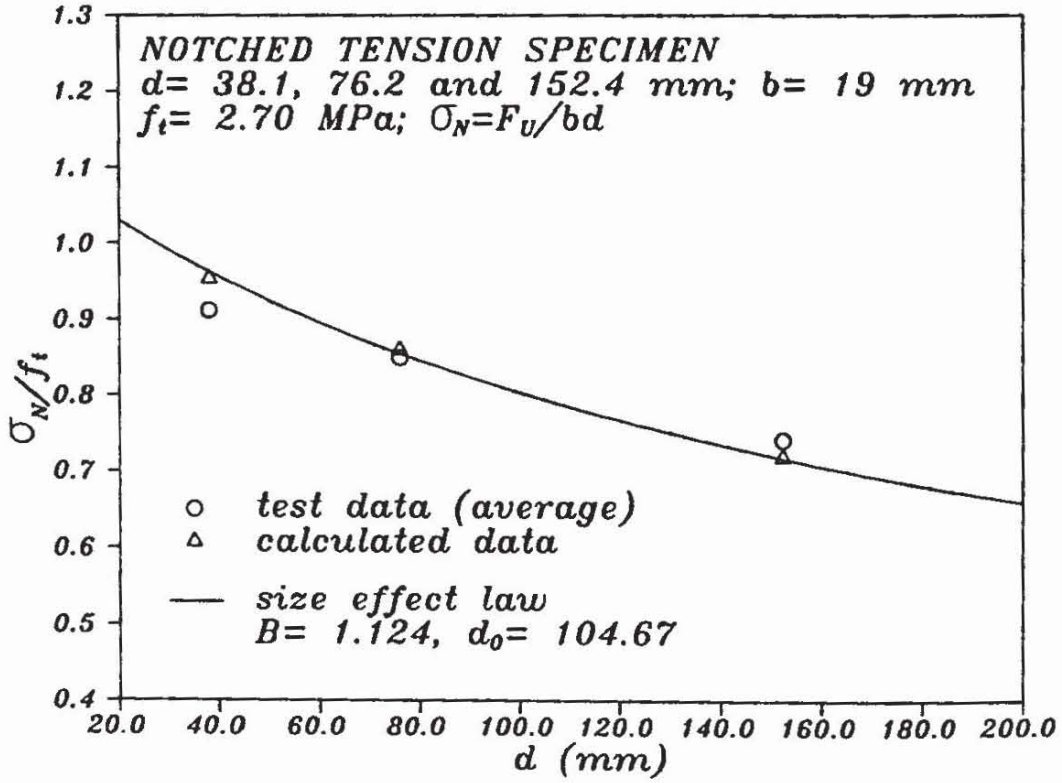

Fig. 6 Comparison between calculated and measured failure loads with size effect law for the notched tension specimen, shown in normal scale.

Fig. 3 that, relative to the specimen size, the fracture process zone decreases with increasing specimen depth. This is a consequence of the fact that the volume of the nonlocal continuum over which the strains are averaged is constant and therefore this volume is, relative to the specimen size, smaller if the size of the specimen is larger.

In Fig. 7 axial strain profiles across the symmetry line of the specimen at the start of the analysis and at peak load are plotted for all sizes. This figure clearly indicates that the strain distribution over the cross-section is more uniform if the size of the specimen is smaller. Therefore with decreasing depth, the stresses in the critical section are more uniformly distributed and the average stress increases.

Summarizing, the size effect can be explained by two effects: (1) The size of the fracture process zone relative to the specimen size decreases with increasing specimen depth; (2) because of (1) the strain and stress distribution becomes less uniform with increasing member depth, resulting in a decrease of the nominal stress at peak load.

Example (2)—The three-point bend specimen shown in Fig. 2(b) was tested by Bažant & Pfeiffer [19], using concrete with maximum

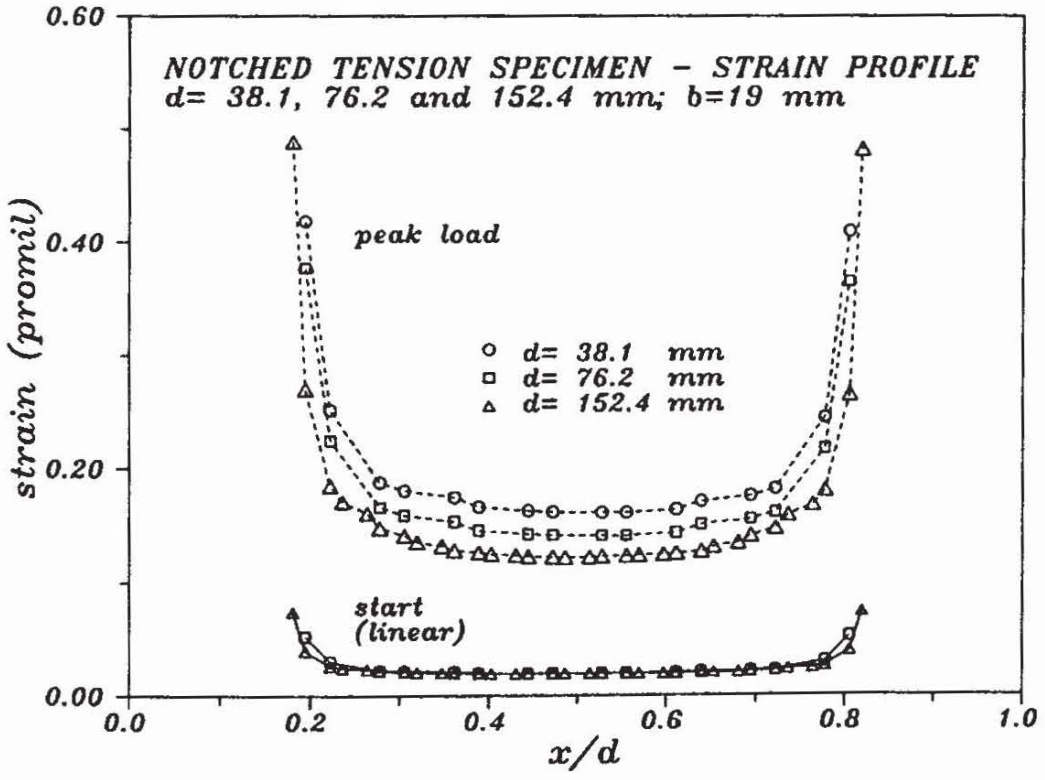

Fig. 7 Strain redistribution in the critical cross-section of the notched tension specimen.

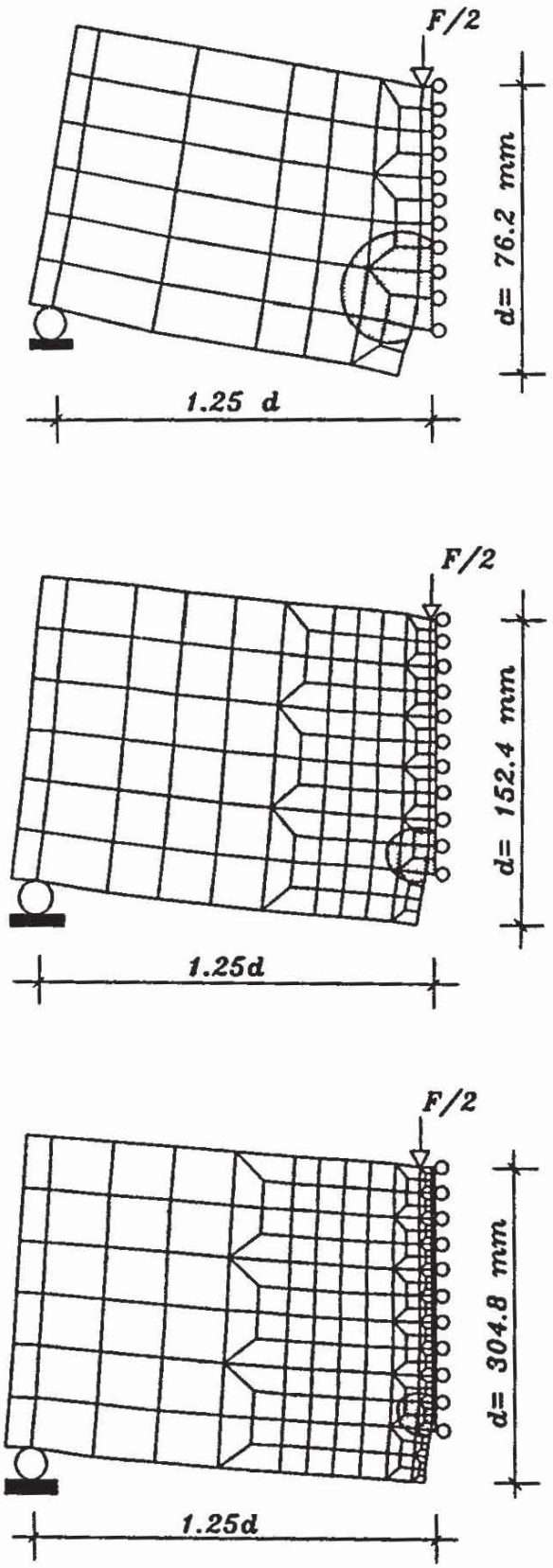

Fig. 8 Deformed finite element meshes and fracture process zone (shaded areas) at peak load for the three-point bend specimen.

aggregate size $d_a = 12{\cdot}7$ mm. The geometry of the specimens basically was the same as in the case of Example (1), except that the depth of the smallest specimen size was $d = 76{\cdot}2$ mm and the thickness of all specimens was $b = 38$ mm. In the analysis, again only one half of the specimen is modelled. The finite element meshes are shown in Fig. 8 in the deformed state. The characteristic length is taken as $l_c = 3d_a$, the microplane model parameters are chosen so that the tension strength is $f_t = 2{\cdot}74$ MPa. In the experiments the average estimated tension strength was $f_t = 2{\cdot}90$ MPa. The material parameters were taken such that the average failure load of the specimen with $d = 152{\cdot}4$ mm is matched.

In Figs 9–11 the nominal bending stresses at peak load according to the theory of elasticity, related to the total depth d, $\sigma_N = 15F_U/(4bd)$, obtained numerically and experimentally are compared with each other and with Bažant's size effect law. Again, calculated results and experimentally measured data exhibit a very strong size effect, well known for bending specimens [20], [21]. According to Fig. 11, the bending strength for a specimen with $d = 76{\cdot}2$ mm is $\sigma_N \simeq 1{\cdot}5f_t$. This relatively small bending strength is due to the notch, because the

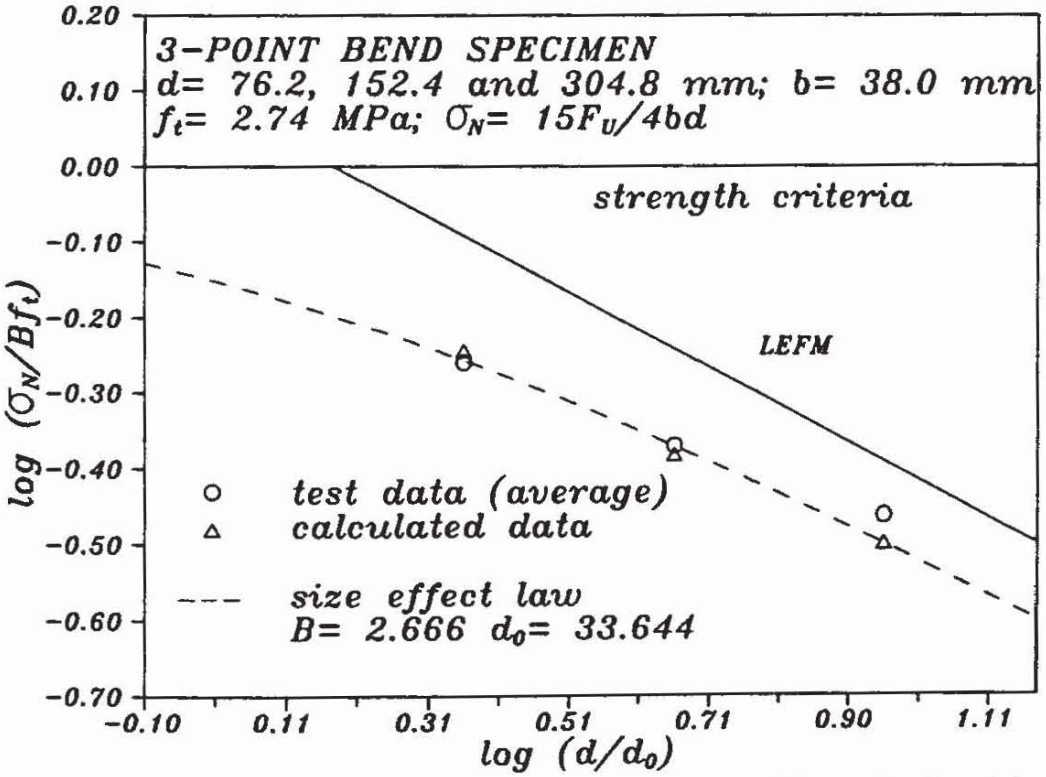

Fig. 9 Comparison between calculated and measured failure loads with size effect law for the three-point bend specimen.

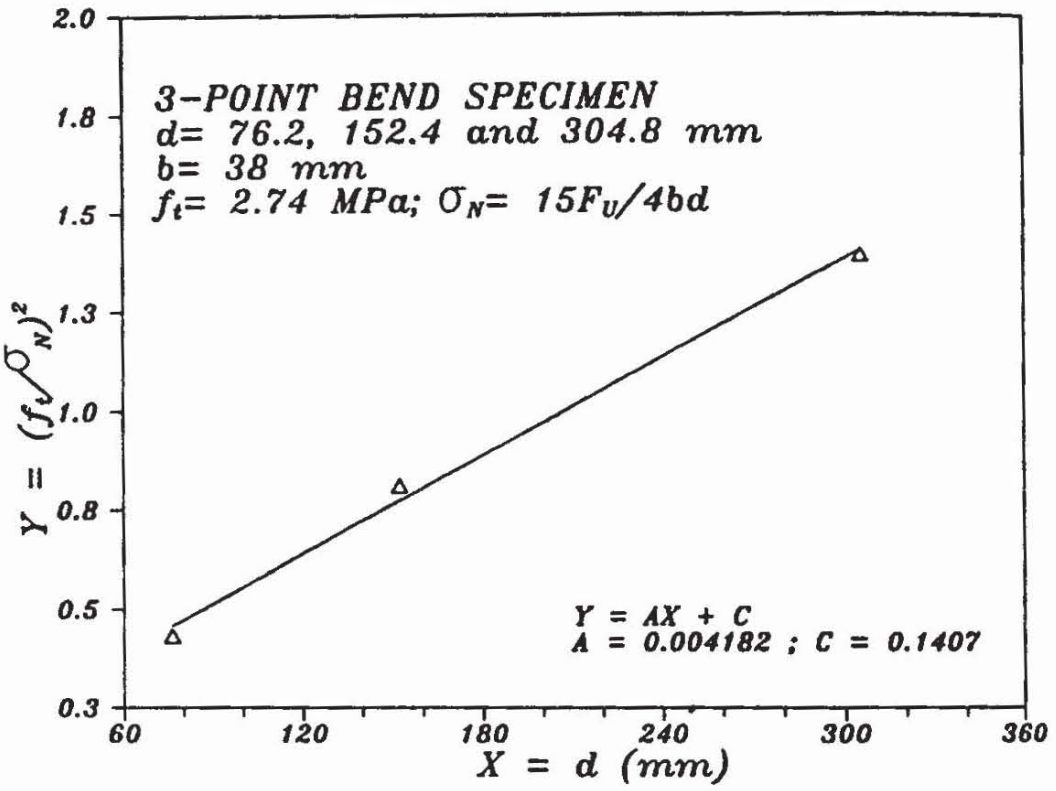

Fig. 10 Linear regression analysis of the calculated peak loads for the three-point bend specimen.

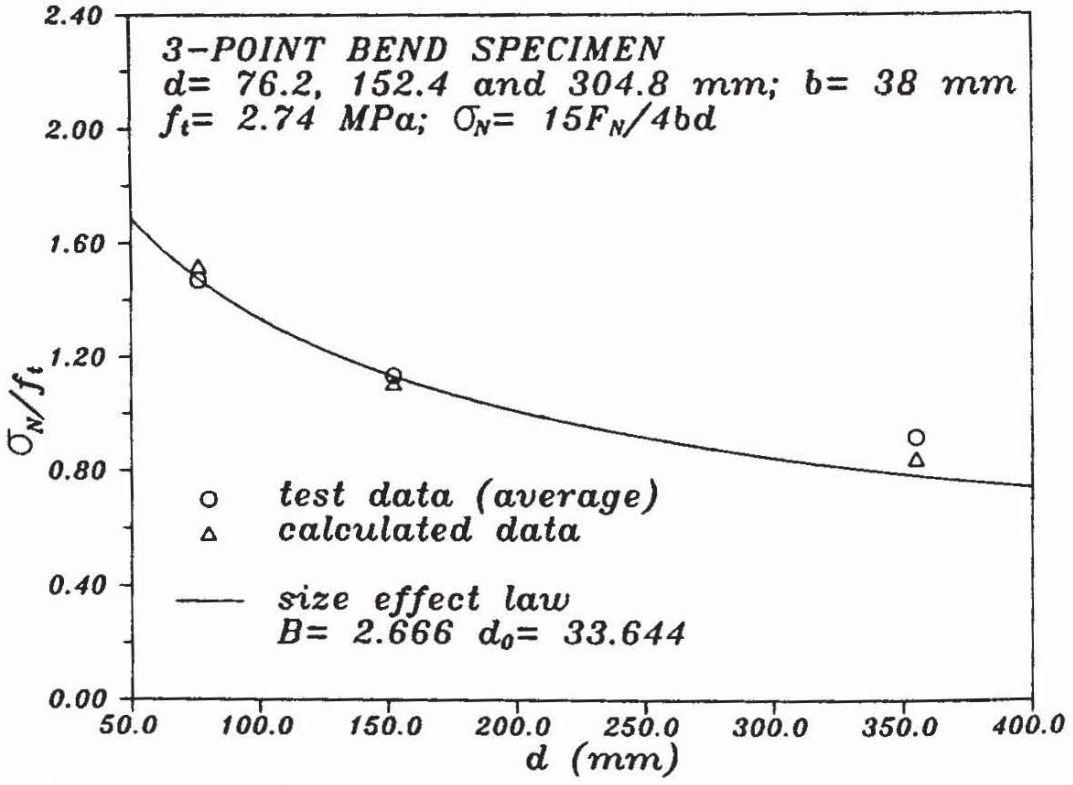

Fig. 11 Comparison between calculated and measured failure loads with size effect law for the three-point bend specimen, shown in normal scale.

strength related to the net area is $\sigma_N \simeq 2{\cdot}15 f_t$ which agrees with the value expected for unnotched beams.

The shaded areas in Fig. 8 indicate the size of the fracture process zones. As in the previous example, the relative size of the fracture process zone decreases with increasing member depth. When, in addition, the strain and stress distribution over the critical cross-section is analysed one comes to the same explanation for the size effect as in the case of the tension specimen. However, the size effect is much more pronounced than in notched tension specimens, because the size of the fracture process zone relative to the member depth is smaller.

In Fig. 12 the nominal bending strengths related to the value for $d = 100$ mm are plotted as a function of the member depth. The numerical values compared are calculated for the net member depth $d_1 = 5/6d$, with predictions according to different proposals valid for unnotched specimens. The test results by Heilmann [20] and Malcov & Karavaev [21], agree rather well. The bending strength decreases from $\sigma_N \simeq 2 f_t$ for $d = 100$ mm to $\sigma_N \simeq 1{\cdot}1 f_t$ for $d = 1000$ mm. According to the CEB Model Code [22] the bending strength is only $\sigma_N \simeq 1{\cdot}5 f_t$ for $d = 100$ mm but approaches $\sigma_N = 1{\cdot}0 f_t$ for larger specimens. The

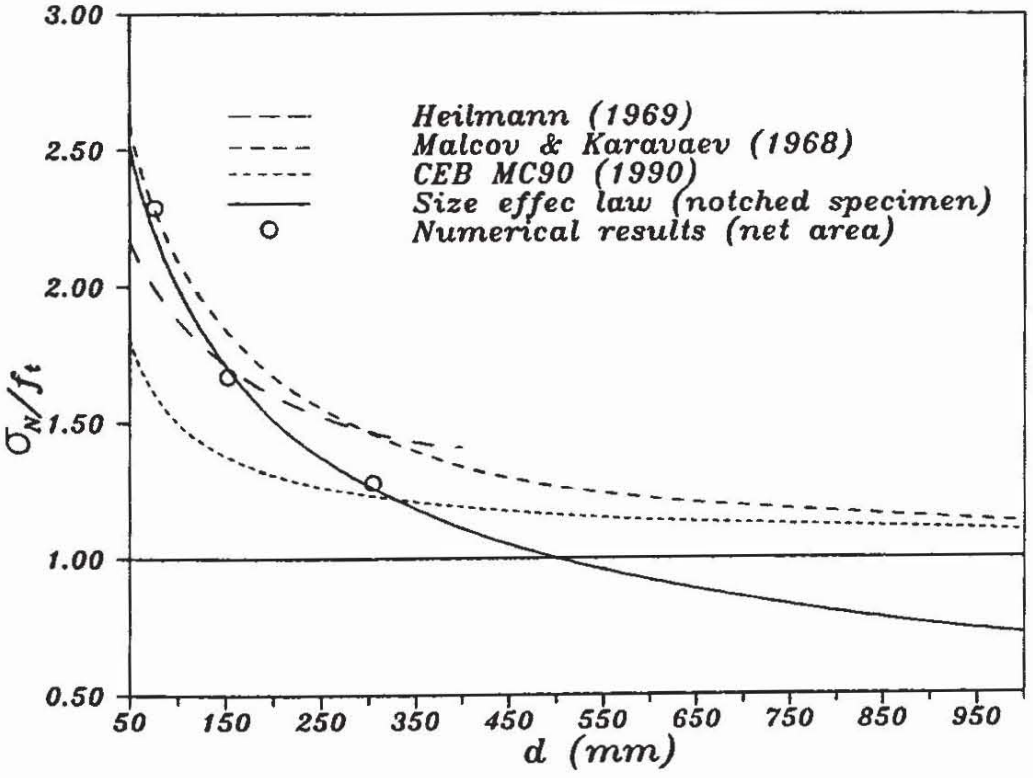

Fig. 12 Relative bending strength as a function of the member depth.

numerical results for notched specimens agree roughly with the other predictions; however, when extrapolating them by the size effect law to larger specimens the nominal bending strength is much lower than the centric tension strength. This is in contradiction to the experimental results for unnotched specimens. This is probably due to the fact that the size effect law was adjusted to fit the results of notched specimens. Therefore unnotched specimens of different sizes should be analysed and the resulting size effect law should be compared with test results.

According to the CEB Model Code 1990 (MC90) [22], the ultimate bending moment of large specimens ($d \gtrsim 1$ m) increases in proportion to d^2. In contrast to this, the size effect law and linear elastic fracture mechanics predict an increase of M_u in proportion to $d^{1.5}$. This means that the failure moment calculated according to MC90 might be unconservative for large specimens.

Example (3)—The concrete cone failure load of headed anchors embedded in a large concrete block is studied. The geometry of the specimen is shown in Fig. 2(c). It is correlated with the embedment depth d. The smallest embedment depth is $d = 50$ mm. The distance between support and anchor is $3d$, so that an unrestricted formation of the failure cone is possible. The axisymmetric finite element mesh, shown in Fig. 13 (deformed shape), is constant in all analysed cases, i.e. the elements are scaled in proportion to d. Contact between anchor and concrete in the direction of loading exists under the head of the anchor only. To account for the restraining effect of the embedded anchor, the displacements of the concrete surface along the anchor in the vicinity of the head are fixed in the direction perpendicular to the load direction. Except at supports, all other nodes at the concrete surface are supposed to be free. Microplane model parameters are taken so that the calculated tension strength is approximately $f_t = 3$ MPa and the uniaxial compression strength is $f_c = 40$ MPa. The characteristic length of the nonlocal continuum is taken as $l_c = 12$ mm. Pulling out of the anchor is performed by prescribing displacements at the bottom of the head.

According to Eligehausen & Ožbolt [18], the concrete cone failure load can be calculated with Bažant's size effect law

$$F_U = F_N B(1+\beta)^{-1/2} \qquad \beta = d/d_0 \tag{2}$$

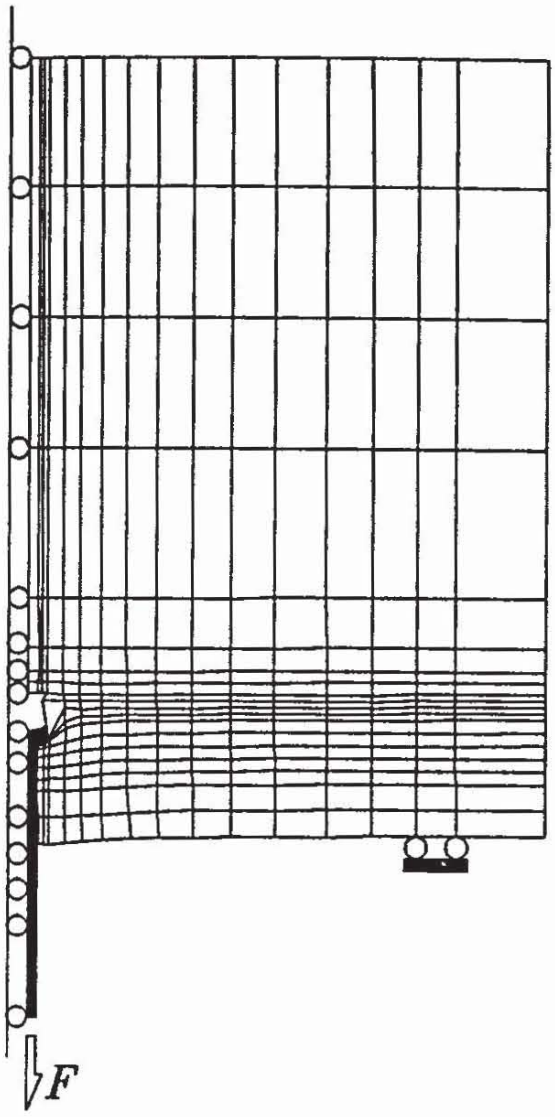

Fig. 13 Finite element mesh for the headed stud specimen, shown in deformed shape at peak load.

where F_U represents load at failure including size effect, F_N a failure load without size effect, and d is embedment depth. B and d_0 are again obtained using linear regression analysis of the numerical results (Fig. 14). F_N, the ultimate load with no size effect, is calculated using the formula

$$F_N = a\sqrt{f_c}\, d^2 \tag{3}$$

where f_c represents the concrete compression strength, a is a factor to calibrate calculated failure loads with measured values and to ensure the dimensional correctness of eqn (3). Equation (3) is proposed by ACI 349, Appendix B (1978) [23], for the prediction of the concrete cone failure load.

In Fig. 15 the results of the analysis are plotted and compared with the size effect law (eqn (2)). The coefficient a in eqn (3) is fixed such

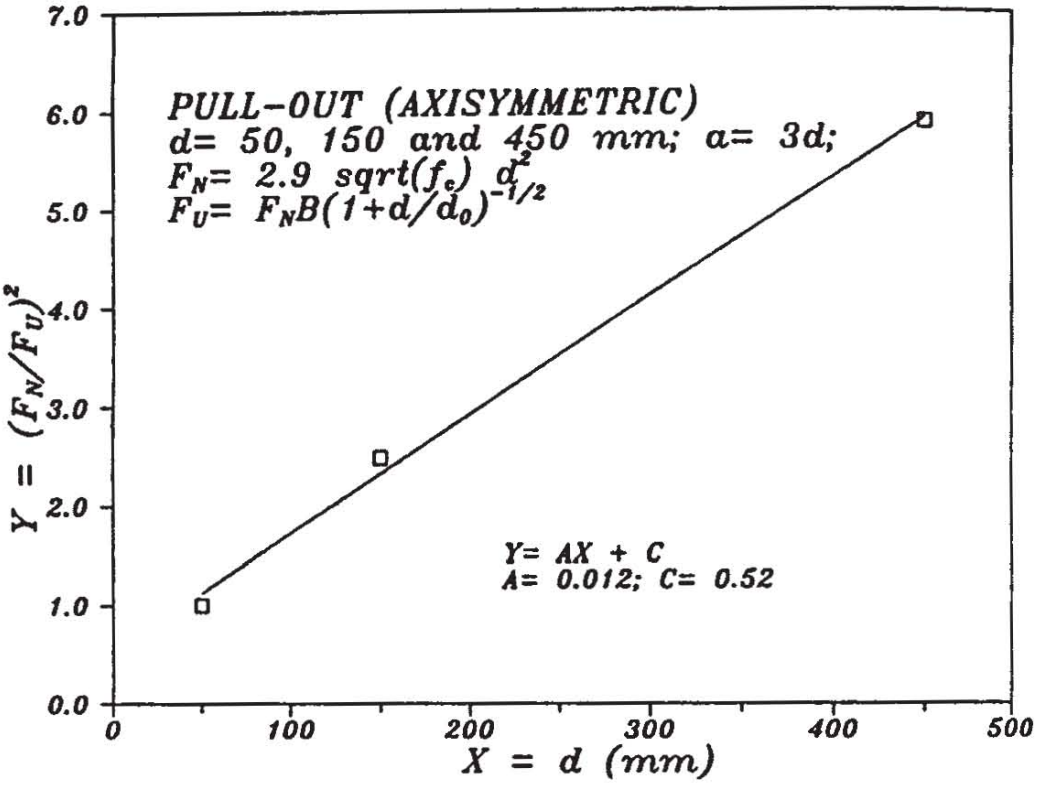

Fig. 14 Linear regression analysis of the calculated peak loads for the headed stud specimen.

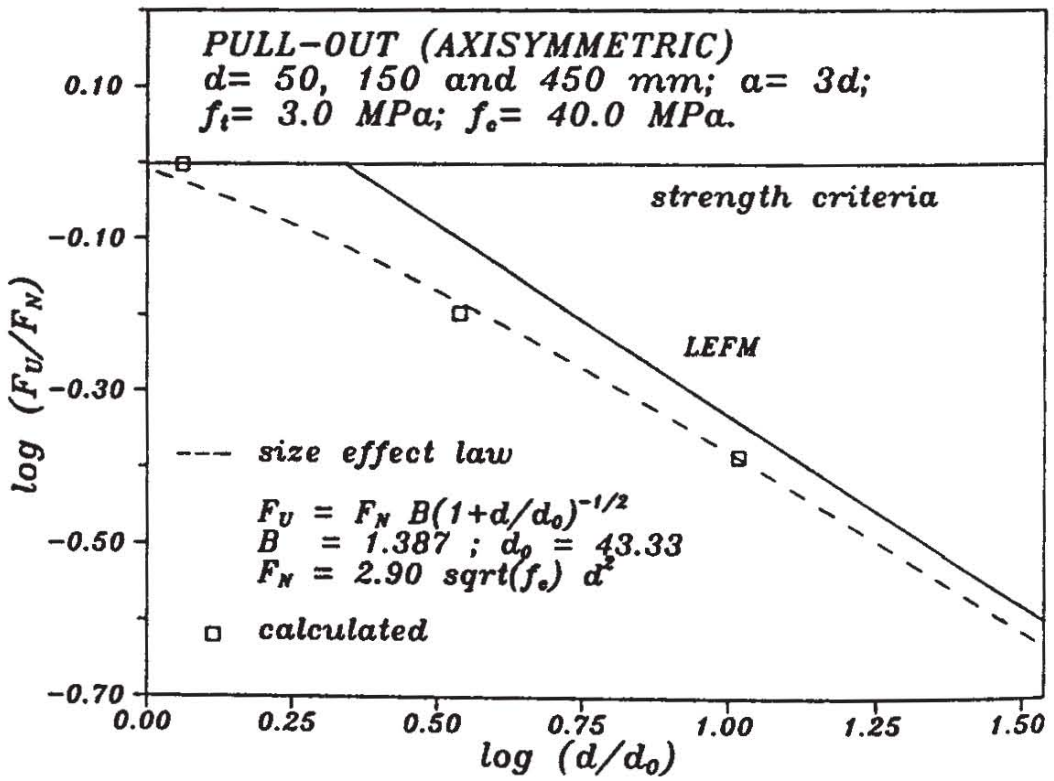

Fig. 15 Comparison between calculated peak loads and size effect law for the headed stud specimen.

that the numerically obtained failure load for anchors with an embedment depth $d = 50$ mm is predicted correctly. As can be seen from Fig. 15, the concrete cone failure loads exhibit a strong size effect, because the numerical results are close to the LEFM solution.

In Fig. 16 the results of the analysis are compared with different failure load equations. The relative failure loads are shown as a function of the embedment depth. The failure load for an embedment depth $d = 150$ mm is taken as the reference value. Plotted are the relative failure loads according to the size effect law (eqn (2)), a formula that neglects the size effect (eqn (3)), and a formula derived on the basis of linear elastic fracture mechanics (eqn (4)) [24]:

$$F_U = a_1 \sqrt{E G_F}\, d^{3/2} \tag{4}$$

In eqn (4), a_1 is a constant and E is Young's modulus. The fracture loads predicted by eqn (4) agree rather well with test results [24]. Assuming no size effect, the failure loads should increase in proportion to d^2, that means by a factor of nine, when tripling the embedment depth. The results of the analysis show that the increase of the failure load is much less (approximately by a factor of 5·7). Therefore the size effect should be taken into account in the design of anchorages, otherwise the failure loads are underestimated for small embedment depths (Fig. 16(a)) and are overestimated for large embedment depths (Fig. 16(b)). The agreement between the size effect formula and the formula based on linear elastic fracture mechanics is good in the entire embedment range. This could be expected on the basis of Fig. 15. The size effect has also been observed in tests by Bode & Hanenkamp [25] and by Eligehausen *et al.* [26]. According to these authors, the failure load increases in proportion to $d^{1.5}$.

The relative shapes of the fracture cone for three different embedment depths, estimated from the numerical analysis at peak load, are plotted in Fig. 17. In Fig. 18 the distribution of the tensile stresses perpendicular to the failure cone surface are shown as a function of the ratio l_h/l_{hmax} where l_h represents the distance from the anchor and l_{hmax} is the failure cone radius taken from Fig. 17. These distributions are estimated from the results of the numerical analysis.

From Figs 17 and 18 the size effect can be explained as follows. With increasing embedment depth the ratio of the diameter of the failure cone to embedment depth decreases, i.e. the effective relative cone surface area decreases as well. Furthermore, the average stress over the failure surface also decreases with increasing embedment depth

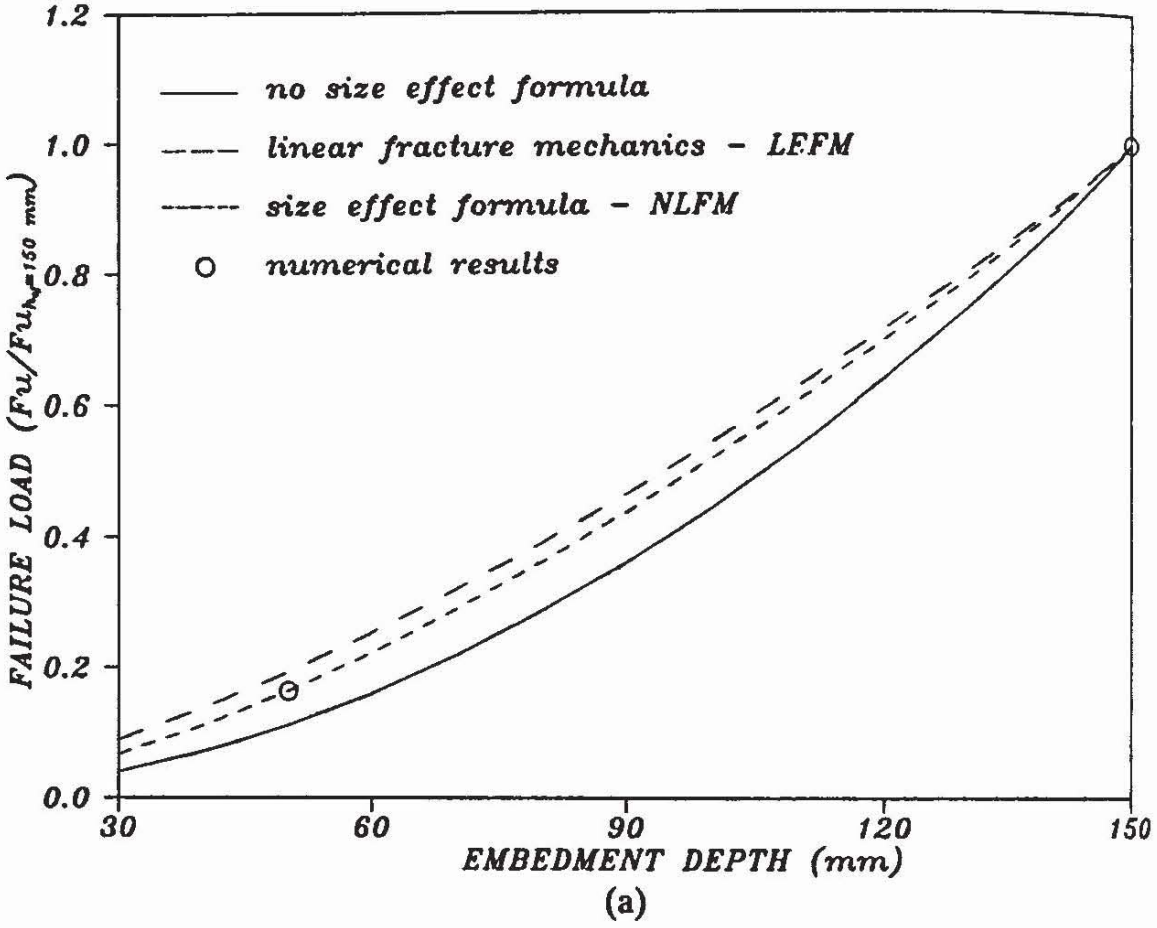

(a)

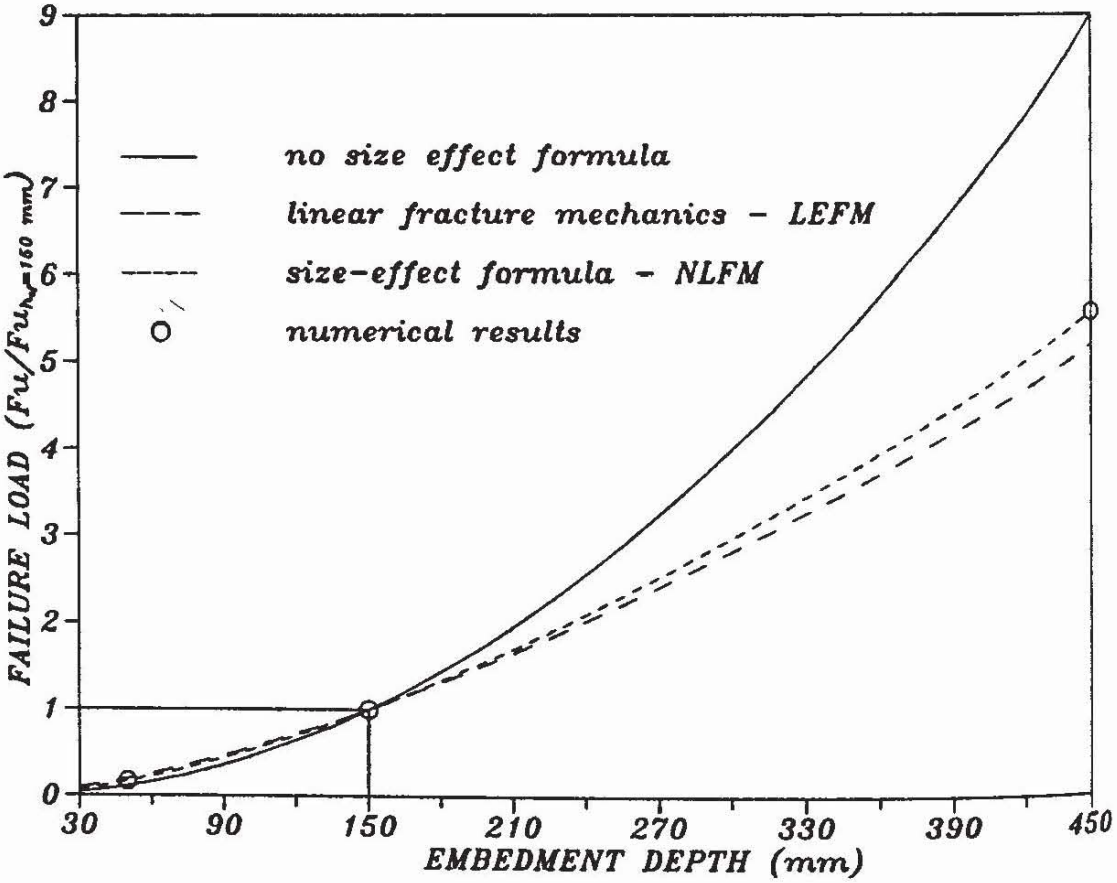

(b)

Fig. 16 Prediction of the failure loads for the headed stud specimen according to different proposals.

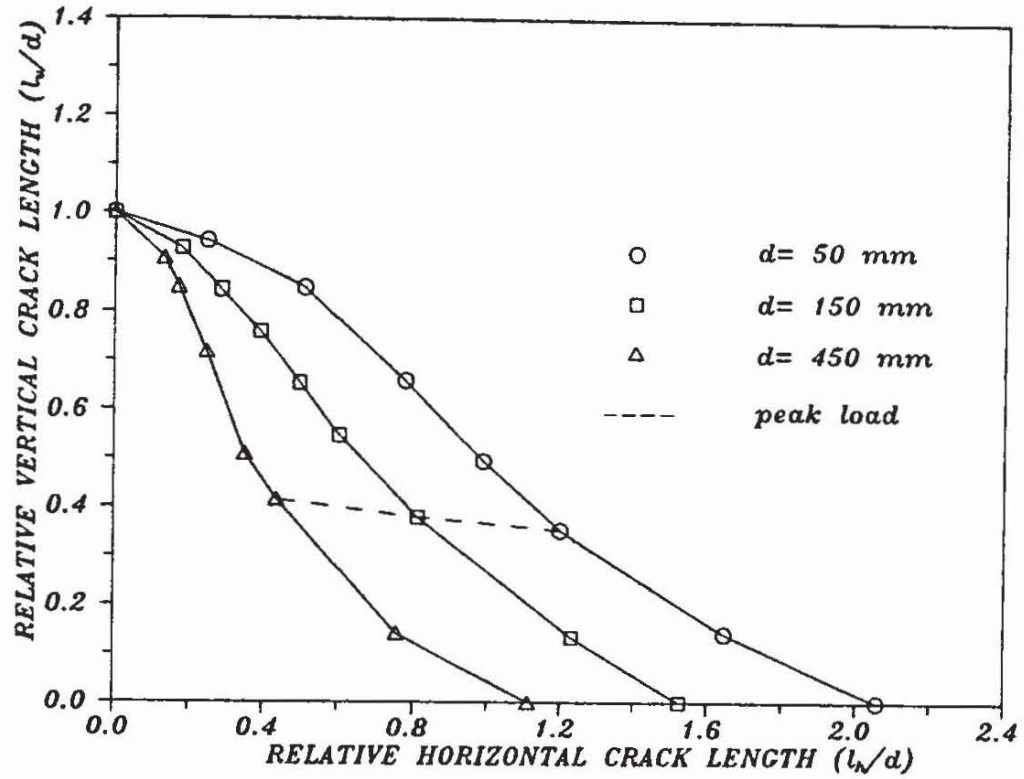

Fig. 17 Shape of the failure cone surface area in axisymmetrical pull-out.

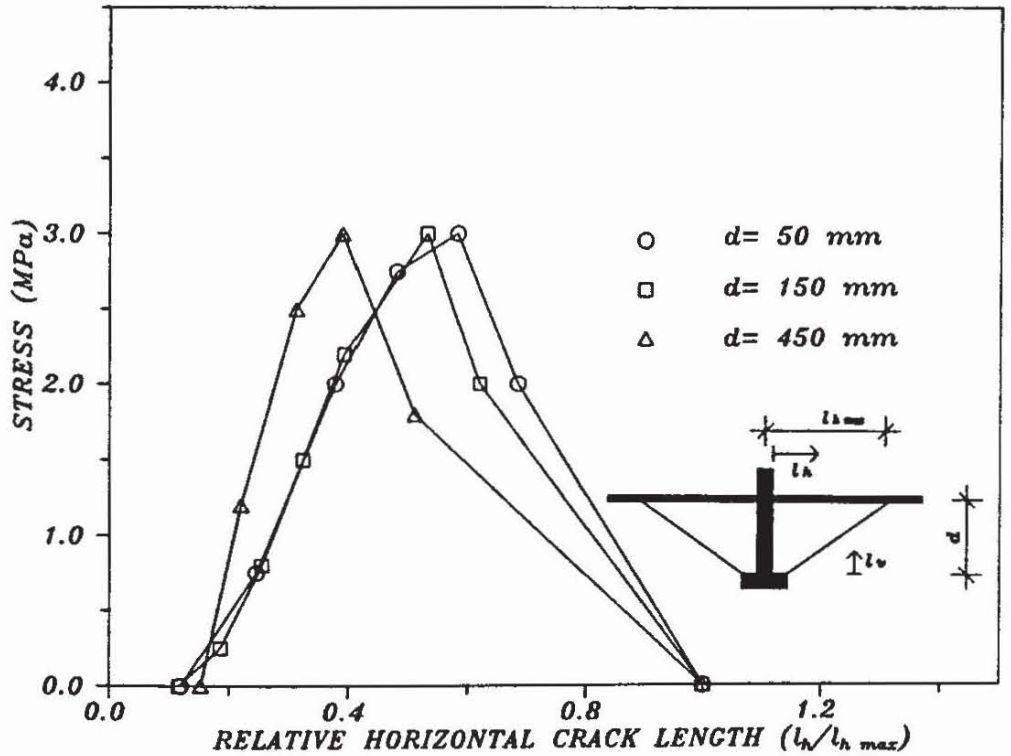

Fig. 18 Tensile stress distribution along the cone surface at peak load in axisymmetric pull-out.

because the stress distribution is more triangular as in the case of a large embedment depth and more parabolic in the case of smaller embedments.

Example (4)—The short beams loaded in torsion (Fig. 2(d)) were tested by Bažant *et al.* [27] using concrete with maximum aggregate size $d_a = 4{\cdot}8$ mm. The depth of the smallest specimen was $d = 38{\cdot}1$ mm. The finite element meshes are plotted in Fig. 19. The same mesh is used for the small and middle-sized specimens (72 finite elements), while for the largest specimen the number of finite elements is increased (176 finite elements). For the beam with $d = 38{\cdot}1$ mm, eight integration points are used in each finite element, while in the middle-sized and the largest specimen 27 integration points are used. To avoid localization due to concentrated loads imposed at the beginning and at the end of the specimen, the first and last cross-sections of the finite element mesh are supposed to behave linear elastically. The characteristic length is taken as $l_c = 15$ mm, the microplane model parameters are chosen so that the calculated tension strength is $f_t = 2{\cdot}60$ MPa and the uniaxial compression strength is

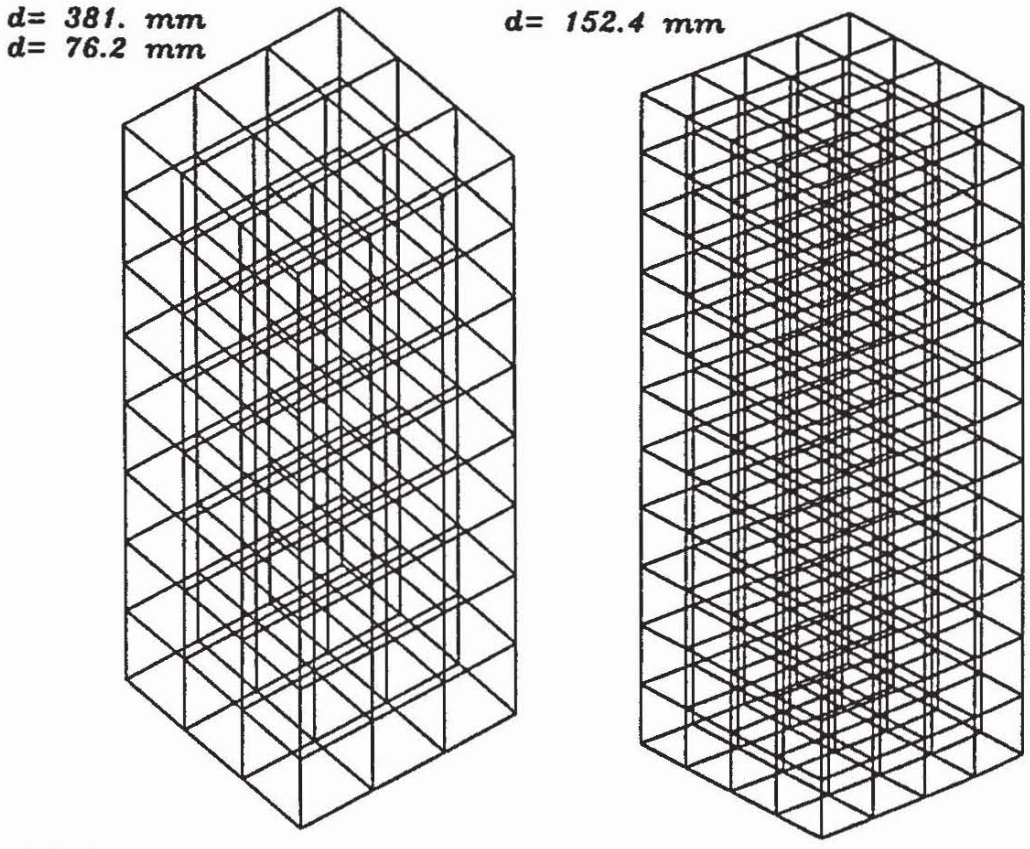

Fig. 19 Finite element meshes used in the analysis of the torsion specimen.

$f_c = 43$ MPa. The average estimated tension strength in the experiments was $f_t = 2{\cdot}70$ MPa. Material model parameters are obtained on the basis of fitting the average experimental failure load for the smallest specimen.

In Fig. 20 the nominal torsion stresses at peak load calculated on the basis of linear elastic theory, $\sigma_N = M_t/(0{\cdot}208d^3)$ with M_t = peak torsion moment, are compared with the average experimental values and the size effect law. The optimum values for the parameters B and d_0 are found by linear regression analysis of the numerical results (Fig. 21). Figure 22 represents a similar comparison in nonlogarithmic scale. As in the previous examples, experimentally and numerically obtained failure loads exhibit significant size effect.

To explain in detail the reason for the size effect in this complicated stress–strain state, further studies are required.

In the present numerical analysis and the tests, the concrete composition was constant. However, note that in practice the maximum aggregate size is not constant, and that for larger structures coarser aggregates are often used. In this case the size effect should be less pronounced than that found in this study. This can be seen from

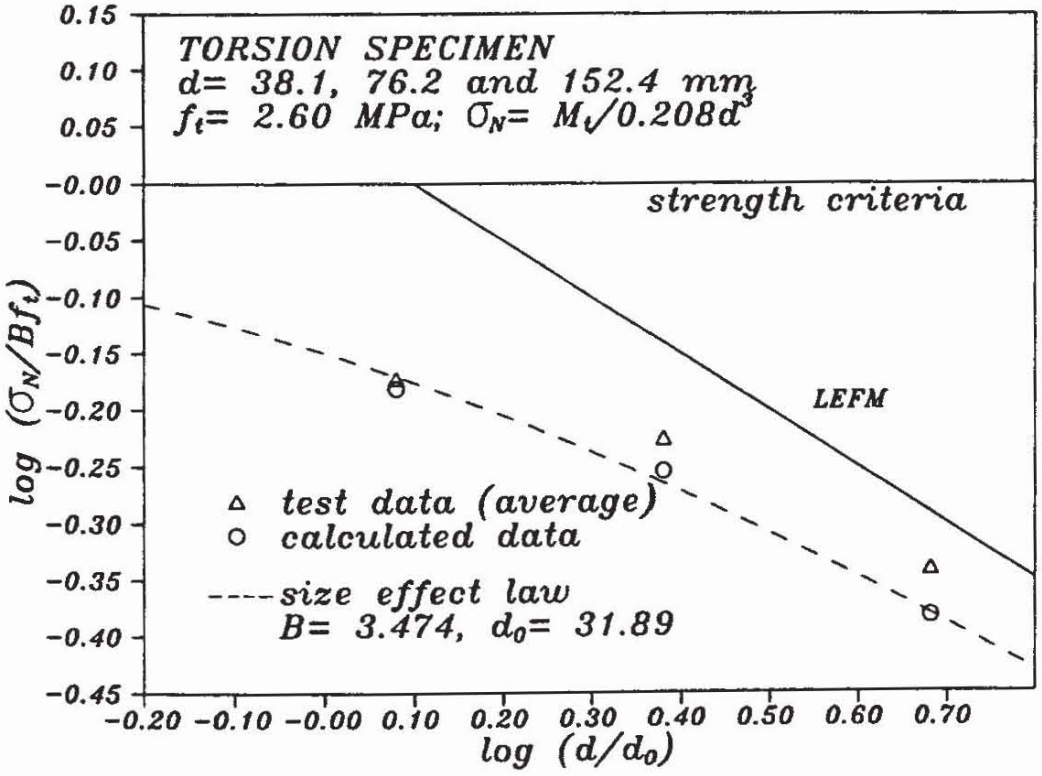

Fig. 20 Comparison between calculated and measured failure loads with size effect law for the beam loaded in torsion.

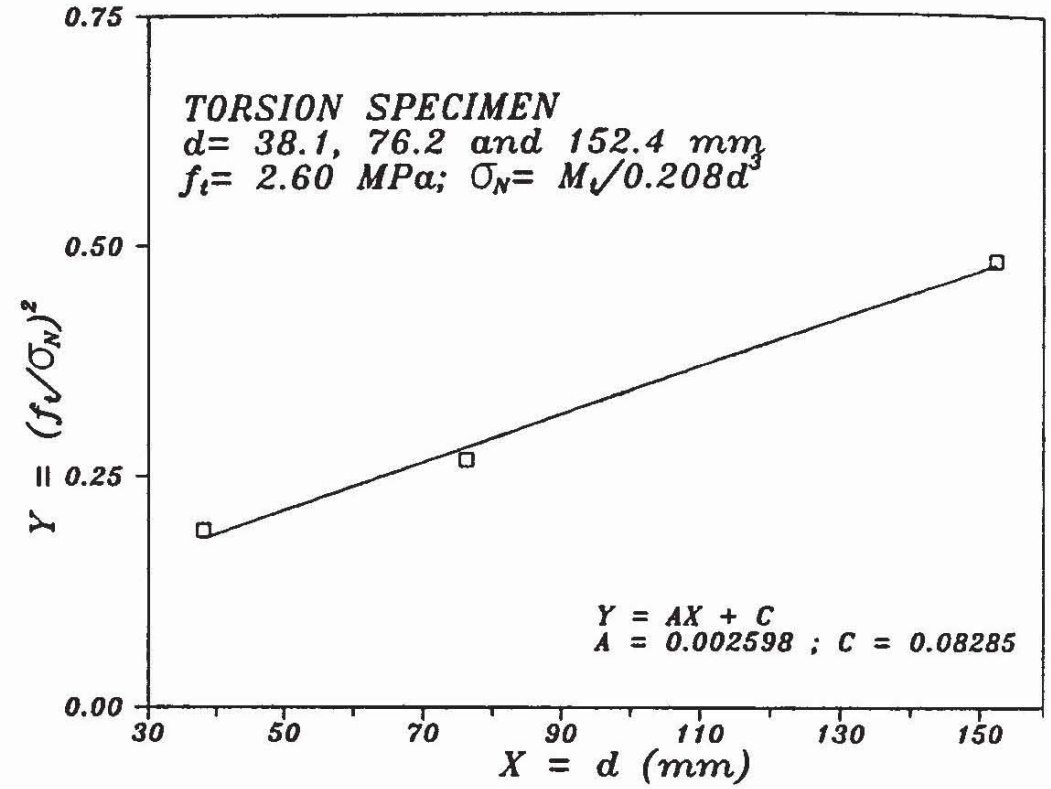

Fig. 21 Linear regression analysis of the calculated peak loads for the beam loaded in torsion.

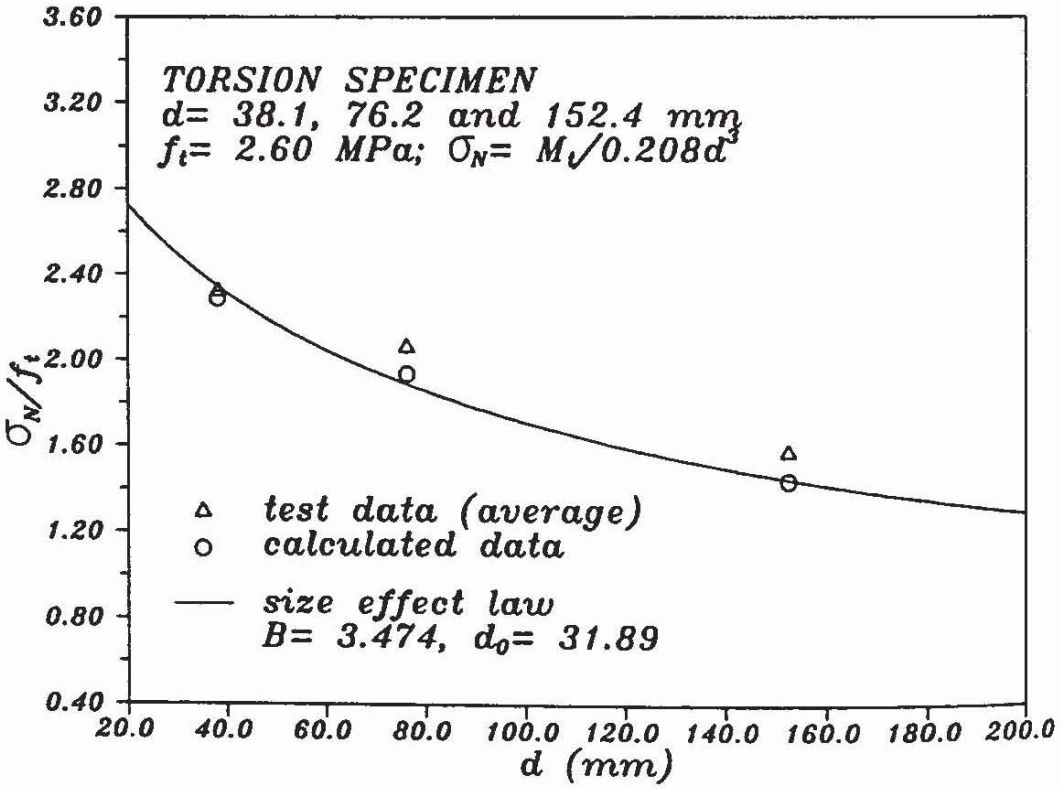

Fig. 22 Comparison between calculated and measured failure loads with size effect law for the beam loaded in torsion, shown in normal scale.

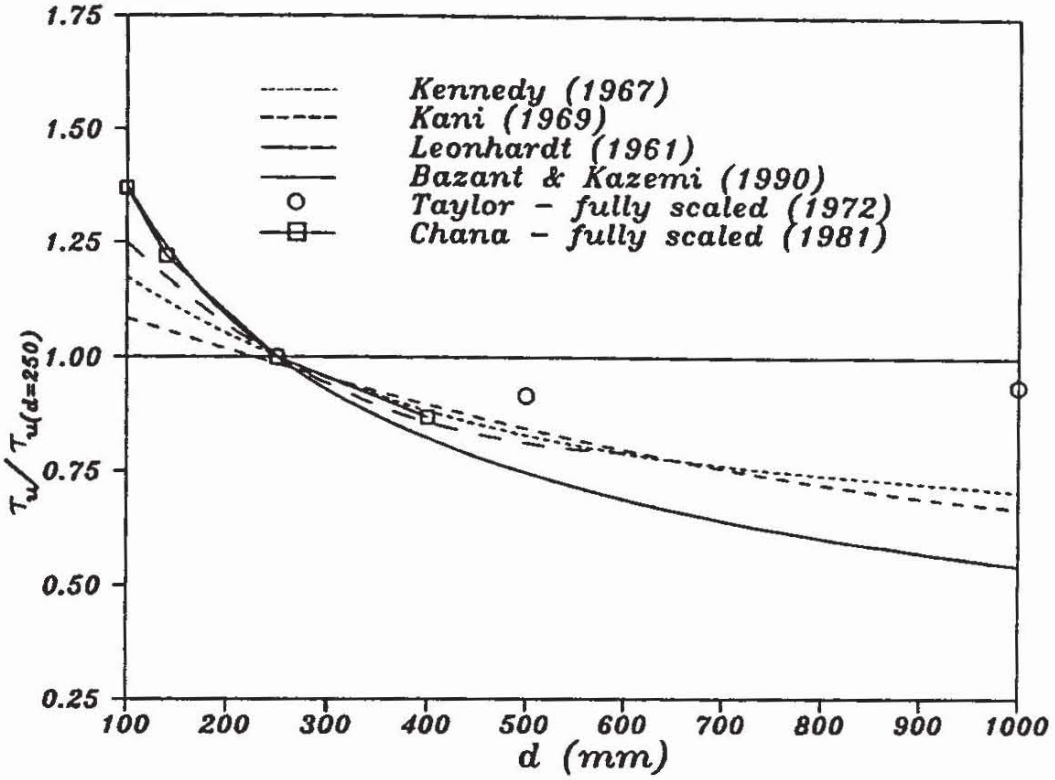

Fig. 23 Relative shear strength of beams without shear reinforcement as a function of the member depth.

Fig. 23 which shows the relative shear stresses at peak load (shear failure) of beams without shear reinforcement as a function of the member depth. The shear strength for slabs with $d = 250$ mm is taken as a reference value. In Fig. 23 test results of Leonhardt & Walter [28], Kani [1] and Kennedy [29] and the size effect law, as proposed by Bažant & Kazemi [30], are plotted. In these investigations the concrete mix was constant. As can be seen, the relative shear strength decreases significantly with increasing member depth. Taylor [31] tested fully scaled specimens that scaled all parameters, including the aggregate size. The shear strength did not decrease significantly with increasing specimen size. However, Chana [32] who also tested fully scaled specimens found that influence of the member depth on the shear strength was almost the same as in the investigations with constant concrete mix.

4. CONCLUSIONS

The results of the present numerical study on the behaviour of plain concrete structures under different loading conditions demonstrate

that the peak loads exhibit a significant size effect. Therefore, the increase of the failure load is much less than the increase of the failure surface area. This is in accordance with experimental evidence. Similar results can be expected in other cases where the concrete tension strength plays a dominant role, such as a bond between deformed reinforcing bars and concrete, frame corners, punching, etc.

The analysis demonstrates that the microplane material model based on the nonlocal strain concept is capable of correctly predicting the behaviour of concrete structures in respect of fracture processes, peak load and size effect. Since the microplane model is a fully 3D material model it can be effectively used in 2D and 3D finite element codes. The fact that in the numerical analysis the size effect is calculated correctly is due to the nonlocal strain concept.

Bažant's size effect law or a suitably simplified formula can predict size effect rather well in a small range of dimensions. But to check this law in a broader range, tests of very large structures are required.

Further studies are needed to clarify the influence of the concrete mix on the size effect. Furthermore, design provisions should be evaluated, which take the practical conditions into account, and which should be incorporated in codes.

The size effect in concrete structures is significant and should be taken into account in the design codes.

REFERENCES

[1] Kani, G. N., How safe are our large concrete beams? *ACI Journal*, Proceedings, **64** (1967) 128–41.

[2] Bažant, Z. P., Size effect in blunt fracture: Concrete, rock, metal. *J. Eng. Mechanics* (ASCE), **110**(4) (1984) 518–35.

[3] Taylor, G. I., Plastic strain in metals. *J. Inst. Metals*, **62** (1983) 307–24.

[4] Batdorf, S. B. & Budianski, B., A Mathematical Theory of Plasticity Based on the Concept of Slip. NACA TN1871, April, 1949.

[5] Zienkiewicz, O. C. & Pande, G. N., Time-dependent multi-laminate model of rocks—a numerical study of deformation and failure of rock masses. *Int. J. Num. Anal. Meth. in Geomechanics*, **1** (1977) 219–47.

[6] Bažant, Z. P. & Gambarova, P. G., Crack shear in concrete: crack band microplane model. *J. Struc. Eng.* (ASCE), **110**(10) (1984) 2015–35.

[7] Bažant, Z. P., Microplane model for strain-controlled inelastic behaviour. In *Mechanics of Engineering Materials*, ed. C. S. Desai & R. H. Gallager. John Wiley & Sons, Chichester and New York, 1984, Chap. 4, pp. 45–59.

[8] Bažant, Z. P. & Oh, B.-H., Microplane model for progressive fracture of concrete and rock. *J. Eng. Mechanics* (ASCE), **111**(4) (1985) 559–82.
[9] Bažant, Z. P. & Prat, P. C., Microplane model for brittle–plastic material—Parts I and II. *J. Eng. Mechanics* (ASCE), **114**(10) (1988) 1672–1702.
[10] Bažant, Z. P. & Pijaudier-Cabot, G., Nonlocal continuum damage, localization instability and convergence. *J. Applied Mechanics* (ASME), **55** (1988) 287–93.
[11] Kröner, E., Interrelations between various branches of continuum mechanics. In *Mech. of Generalized Continua*, ed. E. Kröner. Springer, W. Berlin, 1968, pp. 330–40.
[12] Eringen, A. C. & Edelen, D. G. D., On nonlocal elasticity. *Int. J. Eng. Sci.*, **10** (1972) 233–48.
[13] Krumhansl, J. A., Some considerations of the relations between solid state physics and generalised continuum mechanics. In *Mech. of Generalized Continua*, ed. E. Kröner. Springer, W. Berlin, 1968, pp. 298–331.
[14] Levin, V. M., The relation between mathematical expectation of stress and strain tensor in elastic micro-heterogeneous media. *Prikl. Mat. Mehk.*, **35** (1971) 694–701 (in Russian).
[15] Bažant, Z. P., Belytschko, T. B. & Chang, T. P., Continuum model for strain softening. *J. Eng. Mechanics* (ASCE), **110**(12) (1984) 1666–92.
[16] Bažant, Z. P. & Pijaudier-Cabot, G., Measurement of characteristic length of nonlocal continuum. *J. Eng. Mechanics* (ASCE), **115**(4) (1989) 755–67.
[17] Bažant, Z. P. & Ožbolt, J., Nonlocal microplane model for fracture, damage and size effect in structures. Report 89-10/498n Center for Concrete and Geomaterials, Northwestern University, Evanston, 1989, 33 pp. Also *J. Eng. Mechanics* (ASCE), (in press).
[18] Eligehausen, R. & Ožbolt, J., Size effect in anchorage behaviour. Paper presented at Proceedings of the Eighth European Conference on Fracture—Fracture Behaviour and Design of Materials and Structures, Torino, Italy, 1–5 October 1990.
[19] Bažant, Z. P. & Pfeiffer, P. A., Determination of fracture energy from size effect and brittleness number. *ACI Materials Journal*, **84** (1987) 463–80.
[20] Heilmann, H. G., Beziehungen zwischen Zug—und Druckfestigkeit des Betons. *Beton*, **2** (1969) 68–72 (in German).
[21] Malkov, K. & Karavaev, A., Abhängigkeit der Festigkeit des Betons auf Zug bei Biegung und ausmittiger Belastung von den Querschnittsabemssungen. *Wissenschaftliche Zeitschrift der Technischen Universität Dresden*, **17**(6) (1968) 1545–7.
[22] Comité Euro-International du Beton, CEB-FIP Model Code 1990, First Draft. *Bulletin d'Information Nos 195 and 196*, CEB, Lausanne, March, 1990.
[23] ACI 349-76: Code Requirements for Nuclear Safety Related Concrete Structures. *ACI Journal*, **75** (1978) 329–47.
[24] Eligehausen, R. & Sawade, G., A fracture mechanics based description of the pull-out behavior of headed studs embedded in concrete. *Fracture*

Mechanics of Concrete Structures—RILEM Report, ed. L. Elfgren. Chapman and Hall, London, 1989, pp. 281–99.

[25] Bode, H. & Hanenkamp, W., Zur Tragfähigkeit von Kopbolzen bei Zugbeanspruchung. *Bauingenier*, **60** (1985) 361–7 (in German).

[26] Eligehausen, R., Fuchs, W. & Mayer, B., Tagverhalten von Dübelbefestigungen bei Zugbeanspruchung. *Betonwerk + Fertigteil–Technik*, **12** (1987) 826–32, and **1** (1988) 29–35, (in German and English).

[27] Bažant, Z. P., Sener S. & Prat, P., Size effect test of torsional failure of plain and reinforced concrete beams. *Materials and Structures*, **21** (1980) 425–30.

[28] Leonhardt, F. & Walter, R., Beiträge zur Behandlung der Schubprobleme im Stahlbetonbau, *Beton und Stahlbeton* (Berlin), **56** (12) (1961) and **57** (2, 3, 6, 7, 8) (1962) (in German). The Stuttgart Shear Tests 1961. C. & C. A. Library Translation No. 111, Cement and Concrete Association, London, UK.

[29] Kennedy, R. P., A Statistical Analysis of the Shear Strength of Reinforced Concrete Beams. Technical Report No. 78, Department of Civil Engineering, Stanford University, USA, April 1967.

[30] Bažant, Z. P. & Kazemi, M. T., Size Effect on Diagonal Shear Failure of Beams Without Stirrups. Internal Report, Center for Advanced Cement-Based Materials, Northwestern University, Evanston, USA, 1990.

[31] Taylor, H. P. J., Shear strength of large concrete beams. *J. Struct. Div. Proc. ASCE*, **98** (1972) 2473–91.

[32] Chana, P. S., Some aspects of modelling the behaviour of reinforced concrete under shear loading. Cement and Concrete Association, London, July 1981.